Use of ^{18}F-2-Fluorodeoxyglucose to Label Antibody Fragments for Immuno-Positron Emission Tomography of Pancreatic Cancer

Mohammad Rashidian,[†,⊥] Edmund J. Keliher,[‡] Michael Dougan,[†,§] Patrick K. Juras,[†,⊥] Marco Cavallari,[†] Gregory R. Wojtkiewicz,[‡] Johanne T. Jacobsen,[†] Jerre G. Edens,[†] Jeroen M. J. Tas,[†] Gabriel Victora,[†] Ralph Weissleder,[‡,∥] and Hidde Ploegh*[,†,⊥]

[†]Whitehead Institute for Biomedical Research, Cambridge, Massachusetts 02142, United States

[‡]Center for Systems Biology Department and Department of Radiology, Massachusetts General Hospital, 185 Cambridge Street, Boston, Massachusetts 02114, United States
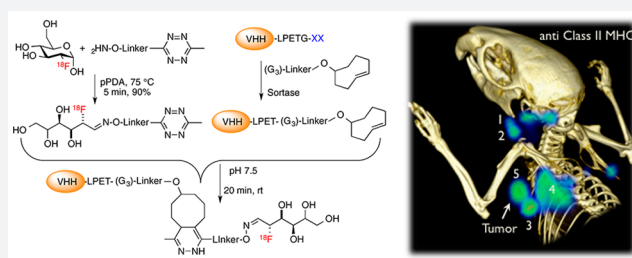
[§]Department of Gastroenterology, Massachusetts General Hospital, 185 Cambridge Street, Boston, Massachusetts 02114, United States

[∥]Department of Systems Biology, Harvard Medical School, 200 Longwood Avenue, Boston, Massachusetts 02115, United States

[⊥]Department of Biology, Massachusetts Institute of Technology, Cambridge, Massachusetts 02142, United States

S *Supporting Information*

ABSTRACT: We generated ^{18}F-labeled antibody fragments for positron emission tomography (PET) imaging using a sortase-mediated reaction to install a *trans*-cyclooctene-functionalized short peptide onto proteins of interest, followed by reaction with a tetrazine-labeled-^{18}F-2-deoxyfluoroglucose (FDG). The method is rapid, robust, and site-specific (radiochemical yields > 25%, not decay corrected). The availability of ^{18}F-2-deoxyfluoroglucose avoids the need for more complicated chemistries used to generate carbon−fluorine bonds. We demonstrate the utility of the method by detecting heterotopic pancreatic tumors in mice by PET, using anti-Class II MHC single domain antibodies. We correlate macroscopic PET images with microscopic two-photon visualization of the tumor. Our approach provides easy access to ^{18}F-labeled antibodies and their fragments at a level of molecular specificity that complements conventional ^{18}F-FDG imaging.

INTRODUCTION

Imaging of medically relevant specimens by positron emission tomography (PET) using ^{18}F-labeled biomolecules is increasingly important for both clinical diagnosis and in biomedical research.[1−7] By exploiting differences in the rate of glucose uptake and its metabolism,[8−11] 2-deoxy-2-^{18}F-fluoroglucose (^{18}F-FDG)-PET imaging can distinguish many tumors with increased metabolic activity from surrounding normal tissue. ^{18}F-Labeled ligands can also be used to track expression of the receptors to which they bind.[2,12,13] While ^{18}F-FDG is readily available in most radiopharmacies, the generation of other ^{18}F-labeled bioactive molecules of interest can require elaborate synthetic strategies.[12−14] A further challenge is the short half-life of [18]F ($t_{1/2}$ = 110 min), which requires use within hours of production. In terms of radiation exposure, the use of ^{18}F-fluorine has advantages over longer-lived isotopes such as [89]Zr ($t_{1/2}$ 3.27 days)[15] and [124]I ($t_{1/2}$ 4.18 days).[16] Use of ^{18}F-FDG is potentially more practical in a clinical setting than are methods using elemental [18]F.[17]

Although antibodies are endowed with exquisite specificity and are of considerable therapeutic value, the use of ^{18}F-labeled antibody fragments has yet to see widespread application for imaging purposes.[18,19] Our approach enables the use of ^{18}F-FDG to achieve efficient labeling of proteins and does so in a manner that is reproducible and site-specific, leaving intact the antibody fragment's antigen binding site. The method also could be applicable to other suitably modified biologicals, such as cytokines and chemokines.[20] The ability to determine the biodistribution of therapeutically useful antibodies or their fragments and a comparison of these measurements with clinical outcomes can thus expand the repertoire of diagnostic tools.

RESULTS AND DISCUSSION

Our strategy relies on a two-step process for labeling proteins equipped with a sortase recognition motif.[21,22] Sortases are bacterial transpeptidases that are finding increasing use as tools for protein engineering. Sortases stand out for their ease of production, high degree of specificity, fast and efficient conversion of the appropriately modified protein substrate,
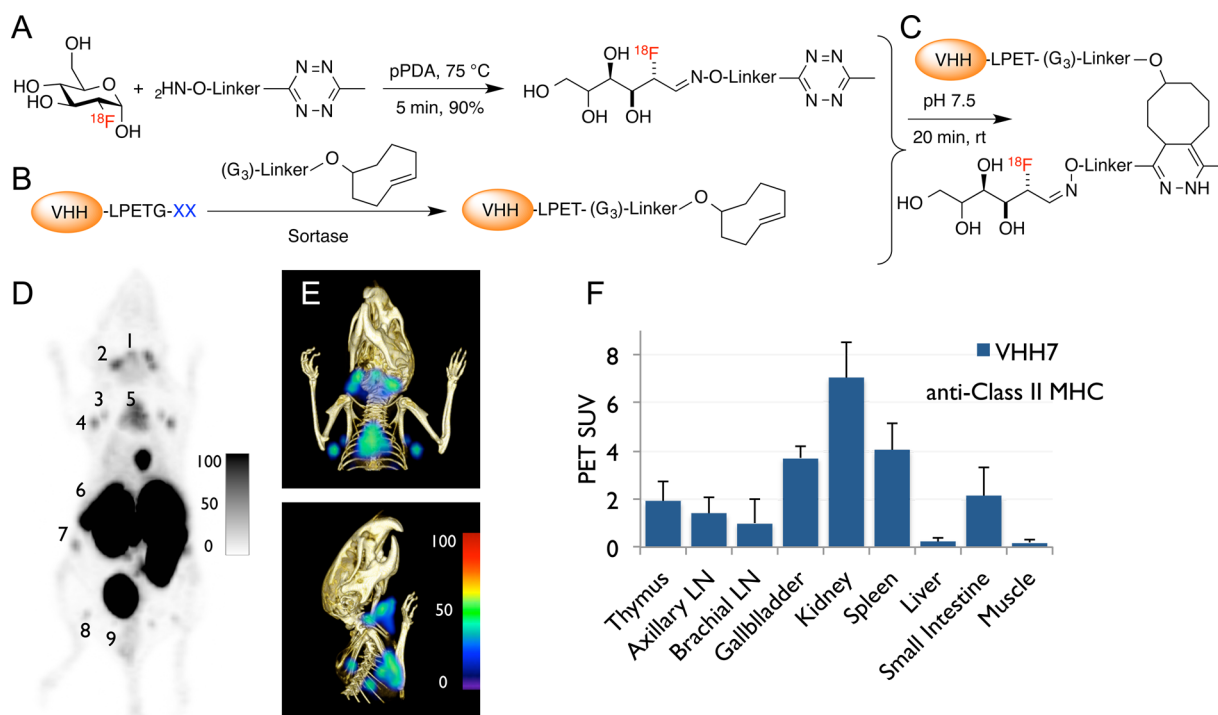
Figure 1. (A–C) Site-specific ^{18}F-labeling of proteins using ^{18}F-FDG and sortase. (A) A tetrazine-aminooxy and ^{18}F-FDG were combined in the presence of *p*-phenylenediamine to produce ^{18}F-tetrazine. Dynamic equilibrium between hemiacetal and linear forms of the aldohexose allows capture of the FDG into a tetrazine molecule via an oxime ligation; the ^{18}F-tetrazine product is purified via HPLC. (B) A single domain antibody fragment (VHH) equipped at its C-terminus with the LPXTG sortase-recognition motif is site-specifically modified with a (Gly)$_3$-*trans*-cyclooctene (TCO), as confirmed by LC-MS (Supporting Information). (C) ^{18}F-Tetrazine was added to the TCO-modified VHH, and after ~20 min the labeled VHH was retrieved by rapid size exclusion chromatography. (D–F) ^{18}F-VHH7 (anti-mouse class II MHC) detects secondary lymphoid organs. (D) PET images of a representative C57BL/6 mouse 2 h postinjection of ^{18}F-VHH7; numbers indicate (i) lymph nodes: 1, 2, 3, 4, 7, 8, 9; (ii) thymus: 5; (iii) spleen: 6. (E) PET-CT images of C57BL/6 mouse imaged with ^{18}F-VHH7 from two different viewpoints (top and bottom panels); clearly lymph nodes and thymus are visible. See movie 01 in Supporting Information for a 3D visualization of lymphoid organs. (F) PET signals *in vivo* in different organs. Experiments are representative of three mice with similar results.

and ready access to a wide variety of nucleophiles in the transacylation reaction.[23−25]

As a first step, we generated a short synthetic peptide, (Gly)$_3$-R, where R contains a *trans*-cyclooctene (TCO) functionality that enables a TCO-tetrazine ligation reaction with a ^{18}F-tetrazine. The TCO-tetrazine reaction is fast, with an estimated second order rate constant of 210−26000 M^{-1} s^{-1}.[26−28] We established a method for ^{18}F labeling using commercially available ^{18}F-FDG, the principal source of ^{18}F in clinical use. The dynamic equilibrium between an aldohexose in its linear aldehyde form (the reactive molecular species) and its cyclical hemiacetal derivative permits the installation of ^{18}F-FDG on an aminooxy-functionalized molecule.[29]

In view of the $t_{1/2}$ of ^{18}F ≈ 110 min, any synthetic process using ^{18}F as a substrate and the necessary downstream purification steps must be rapid. Thus, we first optimized reaction conditions using nonradioactive FDG and characterized the reaction products by liquid chromatography−mass spectrometry (LC−MS) (Supporting Information). Several different catalysts have been reported for the oxime ligation reaction, of which the phenylenediamines are among the most efficient. While *m*-phenylenediamine is a more efficient catalyst than *p*-phenylenediamine (pPDA), its Schiff base is more stable and can block oxime formation if its concentration relative to the aminooxy or aldehyde is high.[30,31] In our case, the concentration of aldehyde (^{18}F-FDG) is extremely low (<nM). We therefore used pPDA as the catalyst at ~0.4−0.6 M and tetrazine-aminooxy in the ~0.2−0.3 M range. We incubated the

aminooxy-tetrazine with fluorodeoxyglucose in the presence of the catalyst, pPDA, with constant agitation at 75 °C for ~5−10 min. High-performance liquid chromatography (HPLC) of the reaction mixture showed (near)-complete consumption of FDG (Supporting Information). To produce the radioactive aminooxy-tetrazine derivative, we performed the incubation with ^{18}F-FDG in the presence of the catalyst, pPDA, with constant agitation at 75 °C for ~5−10 min. Radio-HPLC showed that the coupling reaction with ^{18}F-FDG proceeded rapidly, yielding >90% oxime ^{18}F-FDG-tetrazine in ~5−10 min (Figure 1). We separated the ^{18}F-oxime product by HPLC, followed by capture of the product via a Sep-pak C18 column. A solution containing the TCO-labeled protein of interest, prepared previously using sortase, was then added to the purified oxime ^{18}F-FDG-tetrazine. The reaction was allowed to proceed for ~15−20 min at 25 °C with constant agitation. The ^{18}F-labeled protein was purified by size exclusion in phosphate buffer, providing the final ^{18}F-labeled protein ready for injection.

We previously used a ^{18}F-TCO-tetrazine to label proteins with ^{18}F to image lymphoid organs using an anti-Class II MHC single domain antibody, VHH7.[32] We evaluated the present labeling method to confirm that the binding site of the nanobody remained intact. ^{18}F-VHH7, produced as described above, detected secondary lymphoid organs exactly as reported[32] (Figure 1 and movie 01 in the Supporting Information).
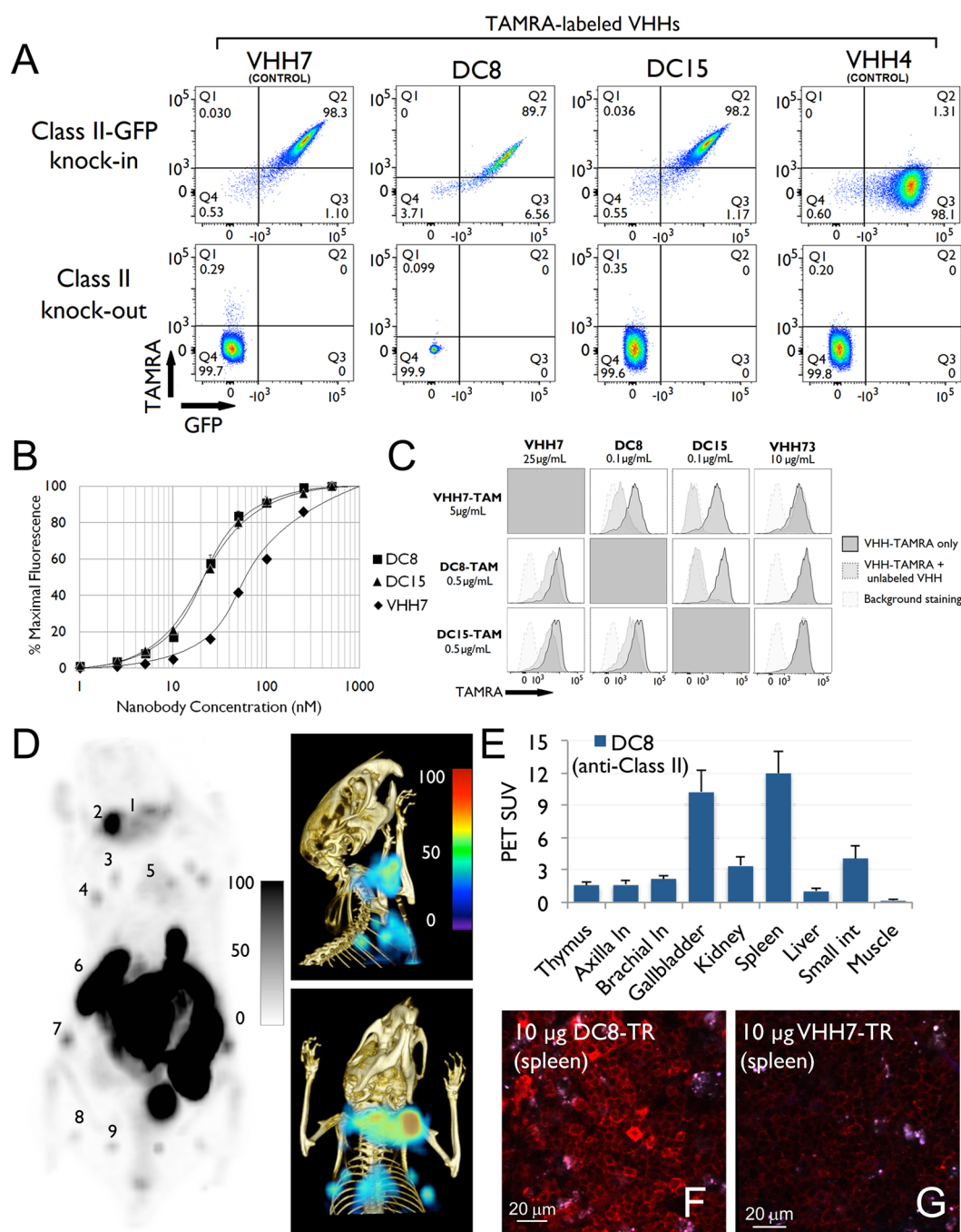
Figure 2. (A) DC8 and DC15 specifically recognize the mouse Class II MHC complex: 10^6 splenocytes isolated from C57BL/6 Class II-GFP knock-in and Class II knockout mice were stained with labeled VHHs as indicated. Plots are gated on live, CD19+ cells. VHH7 has been previously demonstrated to recognize murine Class II MHC. DC8 and DC15 are novel VHHs isolated through staining of dendritic cells. VHH4 is specific for human Class II MHC and does not recognize the murine homologue. (B) DC8 and DC15 are able to stain murine B cells at concentrations too low for VHH7 staining: 10^6 splenocytes isolated from WT C57BL/6 mice were stained with the indicated concentrations of Alexa647-labeled VHHs. Populations were gated on live, CD19+ cells, and the mean Alexa647 fluorescence of each population is plotted. (C) DC8 and DC15 outcompete VHH7 for an overlapping epitope: 10^6 splenocytes isolated from WT C57/BL6 mice were costained with TAMRA-labeled VHH and a variable concentration of unlabeled VHH. The costained splenocytes (dark gray peak) were compared to splenocytes stained only with the TAMRA-labeled nanobody (light gray peak). VHH73 does not bind to class II MHC molecules and is used as a control. (D) ^{18}F-DC8 (anti-mouse class II MHC), produced using ^{18}F-FDG and sortagging, detects secondary lymphoid organs. PET (left) and PET-CT (right-top and bottom) images of a representative C57BL/6 mouse 2 h postinjection of ^{18}F-DC8; clearly lymph nodes, spleen, and thymus are visible. Numbers indicate (i) lymph nodes: 1, 2, 3, 4, 7, 8, 9; (ii) thymus: 5; (iii) spleen: 6. See movie 02 in Supporting Information for a 3D visualization of lymphoid organs. (E) PET signals *in vivo* in all organs. (F, G) DC8 and VHH7 (both anti-mouse class II MHC) stain secondary lymphoid organs with different affinities. Images were acquired using two-photon microscopy. VHHs were site-specifically labeled with Texas Red via sortagging. F and G are images of spleen of C57BL/6 mice injected with 10 μg of DC8-Texas Red (F) or VHH7-Texas Red (G) 90 min prior to imaging. Clearly DC8-Texas Red stains Class II positive cells with higher affinities compared to VHH7. Experiments are representative of three mice with similar results.
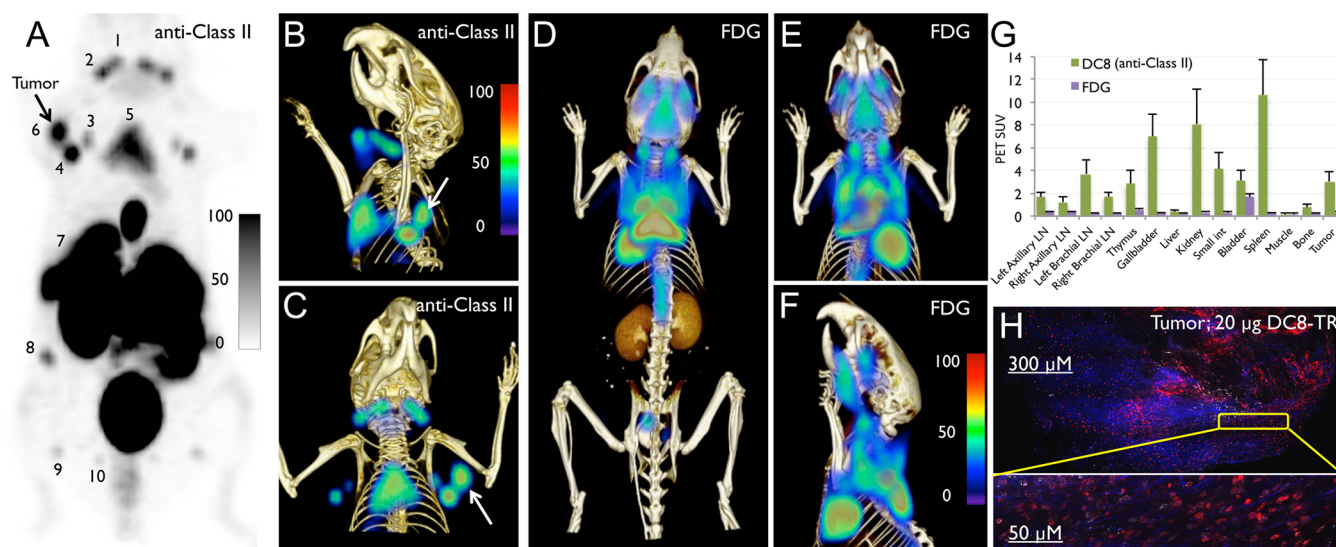
Figure 3. ^{18}F-DC8 (anti mouse Class II MHC) detects infiltration of Class II+ immune cells in/around a tumor. Tumor-associated class II MHC+ cells were visualized using ^{18}F-VHHDC8. A C57BL/6 mouse was inoculated subcutaneously on the back of the left shoulder with 10^6 murine panc02 cancer cells and imaged 2 weeks post injection. (A−C) PET (A) and PET-CT (B, C) images. In A−C, different sets of lymph nodes (1, 2, 3, 4, 8, 9, 10 and their symmetrical counterparts), thymus (5), tumor (6), and spleen (7) are visible. In A−C, as pointed by the arrow, tumor-associated Class II MHC positive cells are visible, attributable to influx of host-derived Class II MHC positive cells. See movie 03 in Supporting Information for a 3D visualization of lymph nodes and tumor-associated Class II MHC positive cells. (D−F) ^{18}F-FDG fails to detect the tumor. A C57BL/6 mouse was inoculated subcutaneously on the back of the left shoulder with 10^6 murine panc02 cancer cells and imaged 2 weeks post injection. ^{18}F-FDG, routinely used in clinic, was used to image tumor-bearing mice. Only highly active tissues (heart, brown fat, mouth muscles) were visible due to their high metabolic activity. The tumor was not visible, probably due to its very small size (∼1.5 mm in diameter) and low metabolic activity. See movie 04 in Supporting Information for a 3D visualization. (G) PET signals *in vivo* in different organs. (H) 2-photon microscopy image of an explanted tumor with MHC class II positive (VHHDC8 stained) infiltrating immune cells. VHHDC8 was site-specifically labeled with Texas Red via sortagging. A C57BL/6 mouse was inoculated subcutaneously on the back of the left shoulder with 10^6 murine panc02 cancer cells. 2 weeks post panc02 cancer cell injection, 20 μg of VHHDC8-Texas Red was injected IV 90 minutes prior to explant imaging of the panc02-tumor. See image 01 in the Supporting Information for high-resolution visualization. Experiments are representative of three mice with similar results.

The half-maximal binding of VHH7 for Class II MHC+ cells on splenocytes is in the ∼55−60 nM range (Figure 2). Possible in vivo applications might benefit from single domain antibodies (VHHs) with improved affinities for their targets. To that end, we identified higher affinity anti-Class II VHHs in a phage display library generated from an alpaca immunized with murine splenocytes. Specificity of the anti Class II VHHs was ascertained by the absence of staining of splenocytes from class II MHC knockout mice, and perfect costaining with GFP-positive cells from class II MHC-GFP knock-in mice[33] using fluorescently labeled VHH derivatives. The affinity of newly identified class II MHC-specific VHHs was compared to that of VHH7. VHHDC8 and VHHDC15 bind ∼3−4 fold better to Class II MHC molecules (Figure 2) than does VHH7. In competition experiments both VHHDC8 and VHHDC15 interfered with each other's ability to bind spleen cells and inhibited binding of VHH7; similarly, an excess of VHH7 inhibited binding of VHHDC8 and VHHDC15 (Figure 2). These findings imply that these different Class II MHC-specific VHHs recognize a closely related epitope.

For *in vivo* analysis, we prepared Texas Red-conjugated VHH7 for comparison with similarly labeled VHHDC8. We injected mice with 10 μg of the Texas Red-conjugated VHHs. Ninety minutes postinjection we excised spleen and lymph nodes for analysis by two-photon microscopy. The signal obtained from VHHDC8-stained lymphoid organs was substantially stronger than that seen for VHH7, indicating that higher affinity for the target improved image intensity (Figure 2). Having established the utility of the new anti-Class II MHC VHH for *in vivo* staining, we used it for PET imaging.

^{18}F-VHHDC8 prepared as described above detected secondary lymphoid organs (Figure 2 and movie 02 in the Supporting Information) in a manner comparable to ^{18}F-VHH7 (Figure 1). Compared to VHH7, we observed stronger binding of VHHDC8 to spleen relative to lymph nodes (compare SUVs in Figures 1 and 2). The higher affinity of VHHDC8 and its short circulatory half-life, typical of a VHH, might lead to its more efficient capture upon passage through the spleen, leaving comparatively less available for exit from the bloodstream and staining of lymph nodes.

Pancreatic tumors are often poorly infiltrated with immune cells and develop a dense stroma, implicated in the resistance to standard chemotherapy and immunomodulatory antitumor treatments.[34] We used the pancreatic cancer cell line Panc02 as a model for pancreatic cancer and explored the possibility of imaging its presence by tracking the arrival of Class II MHC-positive cells (activated host macrophages, dendritic cells) using ^{18}F-VHHDC8. Panc02 itself does not express Class II MHC products. Mice injected subcutaneously with 1×10^6 Panc02 cancer cells were imaged with ^{18}F-VHHDC8 2 weeks after injection of the tumor. Although the tumors were not palpable at the time of imaging (tumor size estimated at ∼1.2 mm in diameter), PET images clearly showed their presence (Figure 3 and movie 03, Supporting Information). PET imaging using ^{18}F-FDG failed to detect the tumor, likely due to its small size and/or low metabolic activity (Figure 3 and movie 04 in the Supporting Information). To correlate the results obtained by PET with microscopy, we injected tumor-bearing mice with 20 μg of Texas Red-VHHDC8. Two hours postinjection, the

tumor was excised and imaged by two-photon microscopy. The tumor was infiltrated with or surrounded by Class II MHC+ cells, consistent with the PET imaging result (Figure 3; see image 01 in the Supporting Information for high resolution visualization).

The short half-life of VHHs (∼10−20 min) likely requires compensation in terms of affinity of the VHH for its target to ensure retention by the tumor. An important limitation of the use of VHHs for immuno-PET is their accumulation in the kidneys and intestine. The use of a longer-lived isotope such as ^{64}Cu or ^{89}Zr might permit an observation window that allows adequate clearance from kidneys and intestine without compromising imaging quality, but this remains to be explored experimentally.

In conclusion, we have site-specifically labeled biomolecules with ^{18}F, starting from a widely available precursor, ^{18}F-FDG. The method avoids the far more demanding generation of carbon−^{18}F bonds and thus facilitates access to ^{18}F-labeled biomolecules, provided these tolerate the presence of a sortase recognition motif, for example, as shown for 4-helix bundle cytokines.[20] We successfully applied immuno-PET to the detection of small heterotopic pancreatic tumor transplants, using high affinity anti-Class II MHC VHHs to decorate the tumor-surrounding immune cells.

The VHH-PET method provides information on the tumor immune microenvironment, while the use of ^{18}F-FDG-PET can identify tumors based on their increased metabolic activity compared to surrounding normal tissue. Both approaches can be applied to the same specimen repeatedly to obtain information on tumor growth and regression, for example, in response to therapy. Immunogenicity of VHHs remains an issue of concern in the case of repeated administration, but approaches for humanization of camelid-derived VHHs have been described[35] to address this issue. The small size of VHHs and their ease of enzymatic modification relative to other formats commonly applied to antibody fragments present a powerful addition to the radiodiagnostic toolbox.[36−38]

ASSOCIATED CONTENT

Ⓢ Supporting Information

The Supporting Information is available free of charge on the ACS Publications website at DOI: 10.1021/acscentsci.5b00121.

  PET-CT movies (ZIP)

  Synthesis and evaluation of the substrates, description of the experiments, and sequences of the VHHs (PDF)
  High-resolution visualization (JPG)

AUTHOR INFORMATION

Corresponding Author
*E-mail: ploegh@wi.mit.edu.

Notes
The authors declare no competing financial interest.

ACKNOWLEDGMENTS

REFERENCES

(1) Quigley, H.; Colloby, S. J.; O'Brien, J. T. PET imaging of brain amyloid in dementia: a review. *Int. J. Geriatr. Psychiatry* **2011**, *26* (10), 991−999.

(2) Clark, C. M.; et al. Use of florbetapir-PET for imaging beta-amyloid pathology. *JAMA, J. Am. Med. Assoc* **2011**, *305* (3), 275−283.

(3) Dijkers, E. C.; et al. Biodistribution of ^{89}Zr-trastuzumab and PET imaging of HER2-positive lesions in patients with metastatic breast cancer. *Clin. Pharmacol. Ther.* **2010**, *87* (5), 586−592.

(4) Pichler, B. J.; Kolb, A.; Nägele, T.; Schlemmer, H.-P. PET/MRI: paving the way for the next generation of clinical multimodality imaging applications. *J. Nucl. Med.* **2010**, *51* (3), 333−336.

(5) Schlemmer, H. P.; Pichler, B. J.; Schmand, M.; Burbar, Z.; Michel, C.; Ladebeck, R.; Jattke, K.; Townsend, D.; Nahmias, C.; Jacob, P. K.; Heiss, W. D.; Claussen, C. D. Simultaneous MR/PET Imaging of the Human Brain: Feasibility Study. *Radiology* **2008**, *248* (3), 1028−1035.

(6) Boellaard, R.; et al. FDG PET and PET/CT: EANM procedure guidelines for tumour PET imaging: version 1.0. *Eur. J. Nucl. Med. Mol. Imaging* **2010**, *37* (1), 181−200.

(7) Weissleder, R. Molecular imaging in cancer. *Science* **2006**, *312* (5777), 1168−1171.

(8) Groheux, D.; et al. Correlation of high ^{18}F-FDG uptake to clinical, pathological and biological prognostic factors in breast cancer. *Eur. J. Nucl. Med. Mol. Imaging* **2011**, *38* (3), 426−435.

(9) Higashi, K.; Clavo, A. C.; Wahl, R. L. Does FDG uptake measure proliferative activity of human cancer cells? In vitro comparison with DNA flow cytometry and tritiated thymidine uptake. *J. Nucl. Med.* **1993**, *34* (3), 414−419.

(10) Huebner, R. H.; et al. A meta-analysis of the literature for whole-body FDG PET detection of recurrent colorectal cancer. *J. Nucl. Med.* **2000**, *41* (7), 1177−1189.

(11) Jadvar, H. Prostate cancer: PET with ^{18}F-FDG, ^{18}F- or ^{11}C-acetate, and ^{18}F- or ^{11}C-choline. *J. Nucl. Med.* **2011**, *52* (1), 81−89.

(12) Wester, H. J.; et al. PET imaging of somatostatin receptors: design, synthesis and preclinical evaluation of a novel ^{18}F-labelled, carbohydrated analogue of octreotide. *Eur. J. Nucl. Med. Mol. Imaging* **2003**, *30* (1), 117−122.

(13) Liu, Q.; et al. ^{18}F-Labeled magnetic-upconversion nano-phosphors via rare-Earth cation-assisted ligand assembly. *ACS Nano* **2011**, *5* (4), 3146−3157.

(14) Liu, S.; et al. ^{18}F-labeled galacto and PEGylated RGD dimers for PET imaging of $\alpha v\beta 3$ integrin expression. *Mol. Imaging Biol.* **2010**, *12* (5), 530−538.

(15) Vosjan, M. J.; et al. Conjugation and radiolabeling of monoclonal antibodies with zirconium-89 for PET imaging using the bifunctional chelate *p*-isothiocyanatobenzyl-desferrioxamine. *Nat. Protoc.* **2010**, *5* (4), 739−743.

(16) Knowles, S. M.; et al. Quantitative ImmunoPET of Prostate Cancer Xenografts with ^{89}Zr- and ^{124}I-Labeled Anti-PSCA A11 minibody. *J. Nucl. Med.* **2014**, *55* (3), 452−459.

(17) Keliher, E. J.; Reiner, T.; Turetsky, A.; Hilderbrand, S. A.; Weissleder, R. High-Yielding, Two-Step ^{18}F Labeling Strategy for ^{18}F-PARP1 Inhibitors. *ChemMedChem* **2011**, *6* (3), 424−427.

(18) Vaidyanathan, G.; Bigner, D. D.; Zalutsky, M. R. Fluorine-18-labeled monoclonal antibody fragments: a potential approach for combining radioimmunoscintigraphy and positron emission tomography. *J. Nucl. Med.* **1992**, *33* (8), 1535−1541.

(19) Cai, W.; et al. PET imaging of colorectal cancer in xenograft-bearing mice by use of an ^{18}F-labeled T84.66 anti-carcinoembryonic antigen diabody. *J. Nucl. Med.* **2007**, *48* (2), 304−310.

(20) Popp, M. W.; Dougan, S. K.; Chuang, T.-Y.; Spooner, E.; Ploegh, H. L. Sortase-catalyzed transformations that improve the properties of cytokines. *Proc. Natl. Acad. Sci.* **2011**, *108* (8), 3169−3174.

(21) Mazmanian, S. K.; Liu, G.; Ton-That, H.; Schneewind, O. *Staphylococcus aureus* Sortase, an Enzyme that Anchors Surface Proteins to the Cell Wall. *Science* **1999**, *285* (5428), 760−763.

(22) Guimaraes, C. P.; et al. Site-specific C-terminal and internal loop labeling of proteins using sortase-mediated reactions. *Nat. Protoc.* **2013**, *8* (9), 1787−1799.

(23) Rashidian, M.; Dozier, J. K.; Distefano, M. D. Enzymatic labeling of proteins: techniques and approaches. *Bioconjugate Chem.* **2013**, *24* (8), 1277−1294.

(24) Strijbis, K.; Spooner, E.; Ploegh, H. L. Protein Ligation in Living Cells Using Sortase. *Traffic* **2012**, *13* (6), 780−789.

(25) Tsukiji, S.; Nagamune, T. Sortase-Mediated Ligation: A Gift from Gram-Positive Bacteria to Protein Engineering. *ChemBioChem* **2009**, *10* (5), 787−798.

(26) Blackman, M. L.; Royzen, M.; Fox, J. M. Tetrazine Ligation: Fast Bioconjugation Based on Inverse-Electron-Demand Diels−Alder Reactivity. *J. Am. Chem. Soc.* **2008**, *130* (41), 13518−13519.

(27) Karver, M. R.; Weissleder, R.; Hilderbrand, S. A. Synthesis and evaluation of a series of 1,2,4,5-tetrazines for bioorthogonal conjugation. *Bioconjugate Chem.* **2011**, *22* (11), 2263−2270.

(28) Karver, M. R.; Weissleder, R.; Hilderbrand, S. A. Bioorthogonal reaction pairs enable simultaneous, selective, multi-target imaging. *Angew. Chem., Int. Ed. Engl.* **2012**, *51* (4), 920−922.

(29) Namavari, M.; et al. A novel method for direct site-specific radiolabeling of peptides using [^{18}F]FDG. *Bioconjugate Chem.* **2009**, *20* (3), 432−436.

(30) Rashidian, M.; et al. A highly efficient catalyst for oxime ligation and hydrazone-oxime exchange suitable for bioconjugation. *Bioconjugate Chem.* **2013**, *24* (3), 333−342.

(31) Wendeler, M.; Grinberg, L.; Wang, X.; Dawson, P. E.; Baca, M. Enhanced catalysis of oxime-based bioconjugations by substituted anilines. *Bioconjugate Chem.* **2014**, *25* (1), 93−101 DOI: 10.1021/bc400380f.

(32) Rashidian, M.; et al. Non-invasive Imaging of Immune Responses. *Proc. Natl. Acad. Sci. U. S. A.* **2015**, *112*, 6146−6151.

(33) Boes, M.; et al. T-cell engagement of dendritic cells rapidly rearranges MHC class II transport. *Nature* **2002**, *418* (6901), 983−988.

(34) Feig, C.; et al. The pancreas cancer microenvironment. *Clin Cancer Res.* **2012**, *18* (16), 4266−4276.

(35) Vincke, C.; et al. General Strategy to Humanize a Camelid Single-domain Antibody and Identification of a Universal Humanized Nanobody Scaffold. *J. Biol. Chem.* **2009**, *284* (5), 3273−3284.

(36) Chakravarty, R.; Goel, S.; Cai, W. Nanobody: the "magic bullet" for molecular imaging? *Theranostics* **2014**, *4* (4), 386−398.

(37) D'Huyvetter, M.; et al. Targeted Radionuclide Therapy with A (177)Lu-labeled Anti-HER2 Nanobody. *Theranostics* **2014**, *4* (7), 708−720.

(38) De Meyer, T.; Muyldermans, S.; Depicker, A. Nanobody-based products as research and diagnostic tools. *Trends Biotechnol.* **2014**, *32* (5), 263−270.